Brazilian Journal of Geophysics 40 (2022), 4, 623-641
Brazilian Geophysical Society
ISSN 2764-8044
DOI: 10.22564/brjg.v40i4.2197

1.5D TIME DOMAIN ELECTROMAGNETIC INVERSION USING GLOBAL OPTIMIZATION METHODS AND PARALLEL PROCESSING

Jorge Luis Abril-Benjumea [1]*, Marcos Rodrigues-Vasconcelos [1], Cassiano Antônio-Bortolozo [2], and Francisco Márcio-Barboza [3]

[1] Universidade Federal da Bahia - UFBA, Geosciences Institute, Salvador, BA, Brazil
[2] Centro Nacional de Monitoramento e Alertas de Desastres Naturais - CEMADEN, São José dos Campos, SP, Brazil
[3]Universidade Federal do Rio Grande do Norte - UFRN, Computing and Technology Department, Natal, RN, Brazil

*Corresponding author email: jlab66@gmail.com

ABSTRACT. An innovative comparative study among three different global optimization methods (GOMs) to invert time domain electromagnetic data (TDEM) was applied in the 1.5D subsurface resistivity imaging. These stochastic methods allow the incorporation of different kinds of constraints in the objective function, due to the easiness of implementation in their algorithms and their computational efficiency. Nevertheless, global optimization methods, like any other based on swarm intelligence, cost much computational time, including problems with a high number of unknown parameters and the forward modeling that involves time-consuming calculations such as Gaver-Stehfest inverse transforms, Hankel transforms, and others. To overcome this difficulty, we developed a parallel pure MPI version of each GOM, allowing the distribution of the computation among several cores of a cluster. The performances of the classic version of particle swarm optimization (PSO), grey wolf optimizer (GWO), and whale optimization algorithm (WOA) using MPI parallelism for solving 1.5D TDEM inverse problems are compared here in a set of synthetic and real data. The principal outcomes show: (1) These GOMs reproduced quite well the distribution of subsurface resistivity, either synthetic models or real data, (2) WOA and PSO exhibited better computational performances, converging first than GWO, (3) WOA provided better performance in the final value achieved of the cost function than PSO and GWO did, and (4) pure MPI parallelism provided a 17x and 50x speed-up in the computation time for both synthetic and real data, respectively. In a better way to classify this comparison, we analyzed the solutions using total variation (TV) and Global smoothness (GS) constraints, to identify smooth and sharp structures. Additionally, we diminished the computational time execution with the parallel solution (MPI version of each stochastic traditional method) against the sequential processing.

Keywords: constrained inversion; TDEM; global optimization methods; parallel computing.

INTRODUCTION

The time domain electromagnetic method (TDEM) or transient electromagnetic (TEM) is a technique that has been used for more than 40 years to image the resistivity distribution in the subsurface. This technique involves the induction of an electric current into the ground generated in most cases by a big transmitter loop sized from tens to hundreds of meters of in length. The easiness of data acquisition and the low cost of field campaigns made these tools useful for several hydrogeological and environmental investigations.

After some data processing, an inversion process is carried out to finally obtain the resistivity model of the studied area. There are many approaches to solving nonlinear inverse problems like the local gradient-based and global search methods. These methods involve the use of constraints in the cost function, to reduce its ill-posed nature (Silva et al., 2001). For the first case, local methods can converge fast but are extremely dependent on a good initial model (Gill et al., 2019). In the last case, global methods do not need a good starting point because the search space is made by trajectories randomly selected until a global minimum is attained. These stochastic methods, also called global optimization methods (GOMs), developed their own techniques to avoid getting stuck in local minima.

Compared to gradient-descent algorithms, GOMs have no restrictions linked to the initial models due to the random nature of the search space, but, unfortunately, are quite time-consuming because several runs are needed to evaluate the cost function (Sen and Stoffa, 1995). Algorithms such as PSO (Kennedy and Eberhart, 1995), along with the grey

wolf optimizer (GWO) (Mirjalili et al., 2014), simulated annealing (SA) (Kirkpatrick et al., 1983) and genetic algorithm (GA) (Goldberg, 1989), have been classified into this group of heuristic algorithms.

In spite of the computational cost, over the last 30 years, GOMs have been employed in the inversion of TDEM data to determine the distribution of resistivity in the subsurface. Monteiro and El-Kaliouby (2010) used SA, PSO, and a local optimization technique in the individual and joint inversion of vertical electrical soundings (VES) and TEM data. Similarly, Cheng et al. (2015) applied the joint inversion of DC resistivity and TDEM data using PSO to detect roadways in a coal mine in the east China, and, for the same purpose, Chandra et al. (2017) and Agarwal et al. (2018) used a GWO to an electrical and gravity-magnetic data set, respectively. Supported by the former case, Li et al. (2018) introduced an improved GWO applied to geophysics inversion, and Godio and Santilano (2018) used the PSO for the inversion of electromagnetic soundings, applied to audio-magnetotelluric (AMT) and magnetotelluric (MT) data. These studies show that PSO and GWO are so far the methods most well-known and used, not only in the TEM data but also in other geophysical methods.

In addition to these traditional methods, the whale optimization algorithm (WOA) founded by Mirjalili and Lewis (2016) is a recent heuristic method and is little used in earth sciences and geophysics. Few works published are restricted to 1D inverse problems such as Abdelazeem et al. (2019) and Liang et al. (2022).

Apart from the 1D aforementioned works, 1.5D and 2D inversions of TEM data using GOMs in geophysics are quite rare and computationally demanding, limiting their use to local optimization methods that use complex derivative calculations to achieve the minimum of the cost function. Keeping in mind the idea of avoiding this complex computing and considering the benefit that GOMs offer to the interpreter, incorporating with easiness several constraints in the cost function and supporting the use of a small computer cluster, the challenge can be overcome.

Based on Barboza et al. (2018), we developed a new comparative study analyzing the performance of parallel canonical versions of WOA, PSO, and GWO to solve the 1.5D TEM nonlinear inversion problem, imposing lateral continuity constraints on the parameters model (e.g., Auken and Christiansen, 2004; Santos, 2004), but following 1D forward modeling in form of the layered models, such as Auken et al. (2005). Particularly, we analyzed the total variation (TV) and global smoothness (GS) constraints in the model parameter vector as a way to infer small discontinuities in the lateral continuity, associated with sharp structures and faults (Loke et al., 2003). To alleviate the high computing cost related to the high number of evaluations of the cost function to achieve a global minimum (Sen and Stoffa, 2013), we developed a parallel MPI implementation of each GOM where assessments are parallelly carried out using numerous MPI workers. The efficiency of each algorithm is conducted through tests with synthetic and real data. In both cases, the outcomes found demonstrated to be efficient in recovering the resistivity model. For the sake of simplicity, we discuss the 1D forward modeling of TEM first, then we explain the 1.5D inversion of TEM and, finally, we focus on addressing some general considerations about the parallel processing scheme used in WOA, PSO, and GWO.

1D Forward Modeling of TEM Data

In this research we used the modeling formulation described in Ingeman-Nielsen and Baumgartner (2006), where the authors describe the calculation of the magnetic field above a horizontally stratified earth assuming that the loop is on the surface (z = 0). The formulation is used for central loop configuration, with the magnetic field in the center of the loop expressed by:

$$H_z = aI\int_0^\infty \left[\frac{2R_1^{TE}u_1\lambda}{R_1^{TE}(k_1^2-k_0^2)+(u_0-u_1)^2} - \frac{1}{2}\right]J_1(\lambda a)\,\lambda d\lambda + \frac{I}{2a} + \frac{I}{(k_1^2-k_0^2)a^3}\left((k_0^2a^2 - 3ik_0a - 3)^{-ik_0a} - (k_1^2a^2 - 3ik_1a - 3)^{-ik_1a}\right) \quad (1)$$

Assuming low frequencies, we can define $k_0 \approx 0$. Then the equation above can be simplified as:

$$H_z = aI\int_0^\infty \left[\frac{2R_1^{TE}u_1\lambda}{R_1^{TE}k_1^2+(\lambda+u_1)^2} - \frac{1}{2}\right]J_1(\lambda a)\,\lambda d\lambda + \frac{I}{2a} - \frac{I}{k_1^2a^3}(3+(k_1^2a^2 - 3ik_1a - 3)^{-ik_0a}) \quad (2)$$

where R_n^{TE} is a function that can be obtained by a recursive relationship as follows:

$$R_n^{TE} = \frac{R_{n+1}^{TE}\varphi_{n+1}^{TE}}{R_{n+1}^{TE}\varphi_{n+1}^{TE}}e^{-2u_nh_n} \quad (3)$$

$$\varphi_{n+1}^{TE} = \frac{\frac{u_n}{z_n}-\frac{u_{n+1}}{z_{n+1}}}{\frac{u_n}{z_n}+\frac{u_{n+1}}{z_{n+1}}} \quad (4)$$

$$\hat{z}_n = i\omega\mu_r \tag{5}$$

$$k_n^2 = \omega^2\epsilon_n - i\omega\mu_n\sigma_n \tag{6}$$

$$u_n = \lambda^2 - k_r^2 \tag{7}$$

where h_n is the thickness of the layer n. For the last layer, denoted by N, which corresponds to the geoelectric basement, we have R_N^{TE} =0. I is the current in the loop; a is the radius of the circular loop; J_1 is the Bessel function of order 1; and λ is the variable of integration.

Since the transient response is a causal function (hz = 0 for t < 0), the response transform in the frequency domain to the time domain can be obtained in the form of a sine or cosine transform. Assuming the field does not vary in the area of the receiving coil, where *b* is the radius of the receiving loop and *n* is the number of turns, the mutual impedance can be expressed as:

$$Z(\tau) = \frac{-2nb^2}{\sigma a^3}\int_0^\infty Im[H_z\frac{2g}{\sigma\mu_0 a^2}]\sin(g\tau)dg \tag{8}$$

where

$$\tau = 2t(\sigma_1\mu_0 a^2)^{-1} \tag{9}$$

$$g = \frac{1}{2}(\sigma_1\mu_0\omega a^2) \tag{10}$$

and σ_1 is the conductivity of the first layer, also calculated using the filters developed by Christensen (1990). Then, the apparent resistivity is expressed by:

$$\rho_a(i) = \left[\frac{\sqrt{\pi}a^2nb^2}{20Z(i)}\right]^{\frac{2}{3}}\left(\frac{\mu_0}{t(i)}\right)^{\frac{5}{3}} \tag{11}$$

where i denotes each instant of time.

Nonlinear inversion of 1.5D TEM data

For the sake of clarifying the 1.5D inversion scheme used in this research, we set a number of TDEM soundings (ns) disposed in a parallel line forming transverses. Each sounding was determined by a certain number of layers (nl) that involves ns×nl resistivity parameters (organized in an array ρ) and ns×(nl-1) thickness parameters (organized in an array **h**) for each layer, forming a total number of parameters N_{par} = ns (nl − 1). In addition, we set the N_{par} as an array that contains all model parameters (**z**) and ($\mathbf{d}^o$) as a vector that contains the total number of observed apparent resistivity measurements (N_{obs}) along the transverse.

Assuming these considerations, we can represent the set of observed apparent resistivity data, that is:

$$\boldsymbol{d}^o = \boldsymbol{d}^p(\boldsymbol{z}) + \xi \qquad \boldsymbol{d}^o = \boldsymbol{d}^p(\boldsymbol{z}) + \xi \tag{12}$$

where $\mathbf{d}^p(\mathbf{z})$ is a vector of the apparent resistivity data predicted, obtained through the TDEM responses of 1D layered models (Anderson, 1982; Sandberg, 1988) and **ξ** is an array of discrepancies. Minimizing the norm of **ξ**, the model parameters (**z**) can be recovered, but it is necessary to incorporate constraints, because the solution becomes unstable. To stable the solution, we define a three-term parametric functional as follows (Barboza et al., 2018):

$$P[\boldsymbol{d}^p(\boldsymbol{z}), \boldsymbol{d}^o(\boldsymbol{z}); \boldsymbol{z}] = \Phi_d[\boldsymbol{d}^p, \boldsymbol{d}^o] + \lambda_p\boldsymbol{C}_p(\boldsymbol{z}) + \lambda_h\boldsymbol{C}_h(\boldsymbol{z}) \tag{13}$$

The equation above details three terms on the right side of the parametric functional P. The first term $\mathbf{\Phi}_d$ corresponds to the vector of discrepancies between observed and calculated data, and the second and third one are the constraints that represent the first-order finite difference matrix for resistivities $\mathbf{C}_\rho$ (**z**) and thickness layers $\mathbf{C}_h$ (**z**) of the same layer, below the neighbor pairs of soundings, respectively. These finite difference matrices are described with more detail in Barboza et al. (2018). Also, in Equation (13), λ_ρ and λ_h are the pair of Lagrange multipliers used to compensate the mismatch between data and the constraints incorporated (Hansen, 1992). In this investigation, we used two constraints for computational modeling with synthetic and field data: (i) the GS constraint, that was used to smooth high heterogeneities between model parameters (deGroot Hedlin and Constable, 1990) and (ii) the TV constraint, that has the opposite effect and allows discontinuous solutions (Bertete-Aguirre et al., 2002). In the next section, it is described in detail the mathematical equations for both constraints.

Mathematical equations of the lateral constraints

Different approaches of inversion have been used for incorporating constraints in the cost function. Within these techniques, lateral continuity constraints (LCC) have been widely used to reduce the effects of high contrasts of the 2D and 3D structures (e.g., Auken and Christiansen, 2004; Santos, 2004). In the case of Auken and Christiansen (2004), it is only used laterally constrained inversion (LCI) with the L_2 norm over the layers and resistivities of the model, resulting in an inappropriate method to detect sharp structures and faults. Keeping in mind this disadvantage, the use of L_1 norm becomes helpful to overcome this issue. In addition, these inversion approaches cannot give us the easiness of modifying the cost function because they are based on local methods. In contrast, GOMs have quite flexibility to modify or incorporate constraints (TV or GS) or any other kind of constraints in the cost function. Below we described both types of constraints.

Global smoothness constraint (GSC)

Based on Equation (13), the Φ_d, $\mathbf{C}_\rho$ and $\mathbf{C}_h$ terms are based on the least squares discrepancies between model parameters, that mean a smooth representation of the physical property to be investigated (Constable et al., 1987). The depiction mentioned above by each term is given as follows:

$$\Phi_d = \frac{1}{N_{obs}|\sigma_d^2|}||\log((\boldsymbol{d}^o) - \log(\boldsymbol{d}^p))||_2^2 \quad (14)$$

$$C_\rho = \frac{1}{[(ns-1)nl]|\sigma_\rho^2|}||\mathbf{D}_\rho[\log(\rho)]||_2^2 \quad (15)$$

$$C_h = \frac{1}{[(ns-1)(nl-1)]|\sigma_h^2|}||\mathbf{D}_h\boldsymbol{h}||_2^2 \quad (16)$$

where $||\cdot||^2_2$ expresses the squared l2-norm and the σ_d^2, σ_ρ^2, σ_h^2 terms on the denominator of Equations. (14), (15) and (16) depict the variances applied to normalize the parametric functional P of Equation (13), during the inversion process. These values can be configured after several simulations of test. Furthermore, the $\mathbf{D}_\rho$ and $\mathbf{D}_h$ operators symbolize the matrices of first-order derivatives, whose sizes are described in detail by Barboza et al. (2018).

Total variation constraint (TVC)

This constraint uses the least absolute discrepancies, which are the opposite behavior for the GS constraint. It promotes some discontinuities between the model parameters, favoring the search of sharp structures and faults (Rudin et al., 1992). The mathematical equations are shown below:

$$\Phi_d = \frac{1}{N_{obs}|\sigma_d^2|^{\frac{1}{2}}}||\log((\boldsymbol{d}^o) - \log(\boldsymbol{d}^p))||_1 \quad (17)$$

$$C_\rho = \frac{1}{[(ns-1)nl]|\sigma_\rho^2|^{\frac{1}{2}}}||\mathbf{D}_\rho[\log(\boldsymbol{\rho})]||_1 \quad (18)$$

$$C_h = \frac{1}{[(ns-1)(nl-1)]|\sigma_h^2|^{\frac{1}{2}}}||\mathbf{D}_h\boldsymbol{h}||_1 \quad (19)$$

where $||\cdot||_1$ expresses the l_1-norm.

Considerations about Global Optimization Methods

Metaheuristic techniques of global optimization such as PSO, GWO and WOA have become well known among scientific communities. All these techniques emulate the social conduct of a group of individuals in nature. WOA, PSO and GWO algorithms find promising regions to locate the global minimum, a common objective among them. To locate this minimum, each algorithm is provided with certain mechanisms that allow them to locate the prey and obtain food in the search space. Keeping in mind this, to know the nature of each algorithm, in this section, we described the principal characteristics and mathematical equations used by each of them and addressed the general stopping condition applied in all simulations.

Particle swarm optimization

This method, implemented by Kennedy and Eberhart (1995), imitates the group conduct of a bevy of entities (birds) which work together to achieve a shared objective (e.g., to search meal). In this pursuit, each entity uses its own experience and the bevy experience to attain the common goal (Kennedy, 2006).

For the case of the PSO algorithm, the search for food is controlled by each particle i, having its position ($\mathbf{z}_i$) and its velocity ($\mathbf{v}_i$) within a search space Π. The performance of each particle is evaluated using Equation (13), which expresses the fitness of the particle positions. The best position reached by the i-th particle (noted as personal best) is depicted by ($\mathbf{p}_i$), whilst the best location reached by nearby particles in the bevy (noted as global best) is depicted by ($\mathbf{g}_i$). Along each iteration k, each particle changes its position corresponding to its recent velocity as in

$$\boldsymbol{v}_i(k+1) = \zeta[\boldsymbol{v}_i(k) + c_1\boldsymbol{r_1}\otimes(\boldsymbol{p}_i - \boldsymbol{z}_i(k)) + c_2\boldsymbol{r_2}\otimes(\boldsymbol{g}_i - \boldsymbol{z}_i(k))] \quad (20)$$

$$\boldsymbol{z}_i(k+1) = \boldsymbol{z}_i(k) + \boldsymbol{v}_i(k+1) \quad (21)$$

where i = 1, 2, . . ., n_{part}; and the parameters χ, c_1 and c_2, r_1 and r_2 are the constriction factor introduced by Clerc (1999), two constants and two random vectors enclosed by [0,1], respectively. The symbol ⊗ implies a point-to-point vector product. After several inversion tests, we configured $\zeta = 0.73$, $c_1 = 2.9$ and $c_2 = 1.2$ for all simulations. Similarly, we defined a number of particles $n_{part} = 12 \times n_p$, being n p the total number of model parameters. Finally, we chose a value of 5000 iterations in all simulations.

Grey wolf optimizer

For almost 10 years, the grey wolf optimizer (GWO) has been widely used for many scientists in different fields of the knowledge, including geophysics (e.g., Chandra et al., 2017; Agarwal et al., 2018; Li et al., 2018). This probabilistic technique introduced by Mirjalili et al. (2014) emulates the social hierarchical behavior and the hunting approach of grey wolves (GW) in nature. The social classification structure is comprised by the alpha, beta, delta, and omega categories of wolves. The best three wolves in the group (alpha, beta, and delta) control the guidance of omega wolves towards to a shared goal (e.g., to find the prey). To achieve this goal, Muro et al. (2011) defined three keys to explain the hunting approach used by the wolves: (i) searching, enchasing, and focusing the prey; (ii) tracking, envolving and suffocating the victim up to it quits moving, and (iii) attacking against the prey. To describe the mathematical expressions of the algorithm, we denote each model in the wolf pack as an iteration of a particular vector:

$$\boldsymbol{z}_i(k) = [z_i{}^1(k), z_i{}^2(k), z_i{}^3(k), \dots, z^f(k), \dots, z_i{}^q(k)]^T, \quad (22)$$

where we determine the bold character to define a vector encompassing q scalar elements that represent the number of parameters (f=1,2,…q), with the subfix i expressing the population number (i=1, 2,…, n_{part}) and k denoting the number of iterations.

To represent alpha, beta, and delta wolves in each iteration we have:

$$\boldsymbol{z}^s(k) = [z^{s1}(k), z^{s2}(k), z^{s3}(k), \dots, z^{sf}(k), \dots, z^{sq}(k)]^T, \quad (23)$$

being s ϵ {α, ß, δ}.

The coefficients of search can be calculated as:

$$a_s(k) = a^f(k).\left(2r_{1s}^f - 1\right)$$
$$c_s^f(k) = 2r_{2s}^f;\ s \in \{\alpha, \beta, \delta\}, \quad (24)$$

where $r^f{}_{1s}$ and $r^f{}_{2s}$ are two random numbers between 0 and 1 and f= 1, …, q. The coefficients $a^f(k)$ are linearly diminished from 2 to 0 during each search process as follow:

$$a_s^f(k) = 2 - \frac{2k}{(k_{max})};\ f = 1,2,\dots,q. \quad (25)$$

After that, it is possible to calculate the distances between the current best position and the best positions of α, ß, and δ wolves as:

$$d_i^{sf} = c_i^{sf}.z_{sf}(k) - z_i^k(k),$$
$$i = 1,2,\dots,n_{part};\ \ s \in \{\alpha, \beta, \delta\} \quad (26)$$

Once computed the distances with the above equation, it can be calculated the best positions of α, ß, δ wolves as follow:

$$z^{sf}(k+1) = z^{sf}(k) - a_s^f(k).d_s^f(k) \quad f = 1,\dots,q;$$
$$i = 1,2,\dots,n_{part};\ s \in \{\alpha, \beta, \delta\} \quad (27)$$

Finally, it is calculated the updated position vector using an arithmetic mean among α, ß vectors and the δ vector as follow:

$$\boldsymbol{z_i}(k) = \frac{\boldsymbol{z^{\alpha}}(k+1) + \boldsymbol{z^{\beta}}(k+1) + \boldsymbol{z^{\delta}}(k+1)}{3}, \quad i = 1,\dots,n_{part}. \quad (28)$$

The coefficient $c_s{}^f(k)$ gives random values between 0 and 2 to allow exploring or attacking the prey. If the value becomes 1, it contributes to hunt the prey and, if the value is greater than 1, it contributes to search the prey. This behavior avoids getting stuck in the local minima.

The prey is attacked when it stops its movement, allowing the attack of grey wolves. During the last iteration when $a^f(k)$ becomes 0, coefficient elements of $a_s{}^f(k)$ are equal to 0. The attack is mathematically modeled diminishing the $a^f(k)$ value. Similarly, with the swarm optimization techniques, the GWO updates its position based on the previous position. This mechanism involves an interchange of information among all individuals that guides everyone to a better position within the search space.

Similarly, to the PSO algorithm, we used a number of particles $n_{part} = 12 \times n_p$, being n_p the total number of model parameters, and addressed a value of 5000 iterations in all simulations.

Whale optimization algorithm

The whale optimization algorithm forms part of the swarm intelligence (SI) algorithms, whose essence is based on nature-inspired behavior of organisms in nature. Introduced and developed by Mirjalili and Lewis (2016), this technique simulates the natural hunting conduct of humpback whales for obtaining food. Its adoption has risen in the last 5 years among different researches comprising several scientific fields (e.g., Chen et al., 2019; Lee and Zhuo, 2021). Particularly, the use of WOA in geophysical applications is very restricted and reduced to a few studies (e.g., Abdelazeem et al., 2019; Liang et al., 2022), in comparison to the well-known PSO and GWO algorithms discussed above.

The WOA is based on three similar phases to explain its functioning: (i) involving the prey, (ii) exploitation (i.e., air-ball net assaulting against the prey) and, (iii) exploration (i.e., the pursuit for the prey). Like the GWO, it is denoted each whale population in a particular iteration as a vector, following the expression:

$$\boldsymbol{z_i}(k) = [z_i^1(k), z_i^2(k), z_i^3(k), \dots, z_i^f(k), \dots, z_i^q(k)\,]^T, \quad (29)$$

where we determine the bold character to define a vector encompassing q scalar elements that represent the number of parameters (f=1,2,…q), with the subfix i expressing the population number (i=1, 2,…,n_{part}) and k denoting the number of iterations.

The first mechanism that simulates the encircling of the prey is computed following the equations:

$$d_i^f = c_i^f . z_f^*(k) - a^f(k).d^f(k), \quad i = 1,2,\dots N, f = 1,\dots,q \quad (30)$$

$$z^f(k+1) = z_f^*(k) - a^f(k).d^f(k), \quad i = 1,2,\dots,N\ f = 1,\dots,q \quad (31)$$

In a specific iteration k, $z_f^*(k)$ is only updated if there is a better solution. The coefficients a and c are denoted as:

$$a^f(k) = a^f(k).\left(2r_1^f - 1\right), \quad c_l^f(k) = 2r_2^f, \quad (32)$$

where r_1^f and r_2^f are two random numbers between 0 and 1, and f=1,…,q.

The attack strategy by bubble net is made following three phases that consist in:

- the shrinking circle phase: in this case, the $a^f(k)$ value is diminished from 2 to 0, allowing a better proximity from the current agent (i.e., agent's best position).
- the spiral shape phase: emulates the spiral movement that whales perform to search the whales' position, following:

$$z^f(k+1) = d'^f_i . e^{bl} \cos 2\pi l + z_f^*(k), \quad i = 1,2,\dots,n_{part}; f = 1,\dots,q.2 \quad (33)$$

$$d'^f_i = z_f^*(k) - z_i^f(k), \quad i = 1,2,\dots,n_{part}; f = 1,\dots,q. \quad (34)$$

where d'^f_i represents the distance between the current agent and the better solution obtained so far; b is a scalar that represents the spiral shape and l is a random number between 0 and 1.

- the attack phase: this step involves a behavior in which there is a probability of 50% to choose either the shrinking circle strategy or the spiral shape strategy. This is computed as:

$$z^f(k+1) = \begin{cases} z_f^*(k) - a^f(k).d'^f_i & if\ p < 0.5 \\ d'^f_i . e^{bl}.\cos 2\pi l + z_f^*(k) & if\ p \geq 0.5 \end{cases} \quad (35)$$

being p a random number between 0 and 1 that indicates the probability to choose the two mechanisms described above.

Finally, the prey search mechanism obeys the exploration and exploitation phases of the algorithm, where $a_k^f(k)$ is used to attack or to avoid the prey. If $a_k^f(k)$ is greater than 1, the search is carried out searching the prey and, if the $a_k^f(k)$ value is less than 1, the bubble-net attack is performed. This behavior is mathematically emulated by:

$$d_i^f = c_i^f z_f^{rand}(k) - z_i^f(k), \quad i = 1,2,\dots,n_{part}; f = 1,\dots,q. \quad (36)$$

$$z^f(k+1) = z_f^{rand}(k) - a^f(k).d^f(k), \quad i = 1,2,\dots,n_{part}; f = 1,\dots,q. \quad (37)$$

being $m_f^{rand}(k)$ a random position vector generated to avoid premature entrapment in the algorithm and d_i^f, is the distance between the random value generated and the best position of the prey. Similarly, with PSO and GWO, we configured 5000 iterations and a number of particles of $n_{part} = 12 \times n_p$, being n_p the total number of parameters for all simulations.

General stopping condition

It exists several rules to determine the general stopping condition when working with GOMs: (i) a predefined maximum number of iterations, (ii) a maximum number of cost function evaluations, and (iii) a break condition which ends the iterating of the algorithm once a specific threshold is reached.

In this research we used the last condition proposed by Bartle (1964), in which a stopping condition is accepted when the difference of the parametric functional P (m) between one previous iteration (k − 1) and the current (k) continues approximately equal, below a determined tolerance δ_P that is:

$$P(\boldsymbol{z})_k = P(\boldsymbol{z})_k - P(\boldsymbol{z})_{k-1} \leq \delta_\rho = 10^{-6} \quad (38)$$

where $\|$ denotes the absolute value, and $P(\mathbf{z})_k$ and $P(\mathbf{z})_{k-1}$ are the best solutions attained in the (k) and (k − 1) iterations, respectively. We configured for all

simulations a N_i = 500, that is the number of iterations in which Equation (31) is fulfilled, and the threshold value as $\delta_P = 10^{-6}$.

Parallel implementation of the GOMs

Given that GOMs need a high number of evaluations of the cost function, it is simple to understand that the use of serial versions would demand a high computational cost. To decrease the processing time, we coded a parallelized classical version of each algorithm (WOA, PSO and GWO). In the parallel code implementation, we used the MPI library to distribute the computing across several processes, following the scheme applied by Metcalfe and Charbonneau (2003), where a master process assigns tasks to other MPI processes (workers) on requirement. To clarify the general functioning of the parallelized code, we established the common terminology "agent" to refer to a whale in WOA, a particle in PSO and a wolf in GWO. Additionally, we used the common nomenclature "specific subroutine" to refer to the principal operations performed in WOA, PSO and GWO, respectively. These operations are well described in section Considerations about Global Optimization Methods.

General functioning of the parallelized code

In general, the functioning of the parallel code begins in the main algorithm, where it is invoked by the master process "specific subroutine". Once the population is created, the agents are distributed among the available worker processes resorting to a subroutine that computes the cost function in parallel (mpi-cost subroutine), sending an agent (one array that contains the model parameters) to each worker process. The subroutine waits for the responses of other workers and sends new agents to each worker once the earlier computation has finished (cost function assessment). A determine worker process will perform the 1.5D forward modeling linked to the agent received and will also evaluate the cost function according to Equation (13). The cost function value returns to a master process and again a worker process becomes available to receive an agent from it. This programming paradigm allows the master process to maintain all worker processes busy in case of not having sufficient agents available to release. Once the cost function value is allocated to the agents in each iteration, the mpi-cost subroutine returns to the "specific subroutine" that executes its own operations.

It is worth to mention that a huge part of the time-consuming inversion process using global optimization methods is due to the evaluation of the cost function. In this programming scheme, each worker process available will evaluate a set of particles (cost function) until the maximum number of particles is allocated in each iteration. Once the algorithm has reached a certain number of iterations (i.e., the stopping criteria is attained), the total execution time is calculated.

Methodology used to set search space and Lagrange multipliers

An important issue related with the inversion results of the 1.5D TEM data has to do with setting the search space for the parameter model, that is the upper and lower bounds in which GOMs take place. To overcome this problem, we performed 1D inversions of TEM soundings, to provide the best range of the search space. The Lagrange multipliers λ_ρ and λ_h in Equation (13) are also an important issue in the inversion. Most common approaches to determine these values are evaluated through the Pareto efficiency (i.e, to choose pair values around the corner closer to the origin), following line searches (e.g., Rawlinson et al., 2006; Barboza et al., 2018).

Nonetheless, this technique is quite influenced by the used model and the normalization values introduced in Equations (14), (15) and 16). For this reason, we opted for the trial-and-error method. Thus, after doing several simulations, it was established a value of 0.01 for both multipliers (λ_r and λ_h) and σ_ρ = 400, σ_d = 0.5, σ_h = 0.5 for the normalization values mentioned above.

Additionally, the same analysis used to configure the Lagrange multipliers and the normalization factors in synthetic data was used to configure the experimental data. We chose a value of 0.01 for both Lagrange multipliers (λ_r and λ_h), and σ_ρ = 100, σ_d = 0.8, and σ_h = 0.5, as the configuration parameters obtained after executing 10 previous inversions.

Synthetic examples

To evaluate the performance of the parallelized versions of WOA, PSO and GWO, we elaborated two synthetic models (Figure 1a and 1b) referred to as models A and B. Both models have layer-cake geometry and represent sedimentary media, considered hydro geological targets. In model A, we elaborated a sedimentary basin having three layers with 100Ω.m (yellow color), 50Ω.m (green color) and 500Ω.m (dark brown color) resistivity values. The basin has a very slight slope (< 5%), where the lateral distance between neighboring soundings is larger than the vertical depth. In model B, we created a glacial model, emulating a paleochannel model (Auken et al., 2008). The valley is engraved into melt-water sand with medium to high resistivity of 80 Ω.m (blue color), filled with glacio-lacustrine clay with a resistivity value of 20 Ω.m (yellow color), and covered all by clay with a resistivity value of up to 10 Ω.m (dark blue color). TDEM soundings in 21 sites separated by 200 m were generated using a 2D finite-volume forward modeling code (Cockett et al., 2015), for model A and 16 sites separated by 100 m for model B. Also, we corrupted the synthetic data with Gaussian random noise with zero mean and standard deviation of 2.5% in the data.

Figures 1c and 1d show pseudo-sections of apparent resistivity, for model A and B, respectively. For both models, the apparent resistivity data were carried out using a central-loop configuration with a

loop-size of 100 m, receiver coil area of 14.14 m^2, and with a time range of 0.146-5.21 ms. Additionally, all inversion results were interpreted using 105 and 80 parameters for models A and B, respectively.

Since the parallel versions of WOA, PSO and GWO allow us to run the inversions in an efficient way, we carried out 10 separate simulations. The mean value of the outcomes of those simulations is taken as the final solution. To select the number of agents that make up the population in WOA, PSO or GWO, we first used the strategies proposed by Engelbrecht (2007) and Martínez et al. (2010). Attending these authors, we carried out the test using factors of 6, 8, 10 and 12 times, the number of model parameters to configure the number of agents in the population. We chose to use 1000 agents for the experiments with both data set. Below, it can be found the outcomes for the two synthetic models elaborated for testing the performance of the parallel WOA, PSO and GWO algorithms. In both cases, to assure that the termination criterion be attained (N_i = 500), we kept 5000 iterations as the maximum range of iterations allowed.

Model A: Sedimentary Basin

In Figure 1a it is shown the true model used to build the Sedimentary basin, simulated in this work. The inversion outcomes obtained for this model using the parallelized versions of WOA, PSO and GWO are shown in Figure 2. We concluded that both constraints used to image the subsurface reproduce quite well the true model. On the other hand, we also evaluated the inversion results obtained for the Buried Valley model (model B), shown in Figure 3, that will be discussed in the next section.

To check the quality of both calculated data and the best model solution, we performed an analysis of the cumulative distribution frequency on the relative errors (RE) (%) of the apparent resistivity data and inverted model parameters.

The study shows that almost 85% of the inverted parameter models are reproduced with a value of RE=15% (Figure 4a) for the TV constraint, whilst almost 80% of these inverted parameters are reproduced with a value of RE=10% (Figure 4b) for the GS constraint. It is worth saying that in almost all cases the reproduced data with both constraints present the worst performance with GWO in relation to the WOA and PSO algorithms. It is also possible to infer that almost 90% of the apparent resistivity data achieved RE values lower than 10% for the TV constraint (Figure 5a) and RE values less than 5% for the GS constraint (Figure 5b). It is noted that the GS constraint achieves the best results due to the smooth nature of the model.

Additionally, Figure 6 shows the evolution curves of the cost function for the parallelized versions of WOA, PSO and GWO, using both constraints (for one of the 10 inversions). From the analysis of the figure, we can infer that the GWO required more iterations to converge than the WOA and PSO did. Also, we can conclude that the GS constraint needed less iterations to satisfy the termination criterion defined in Equation (31).

As a complementary analysis of the outcomes presented above, we decided to evaluate the quality of them using a confidence interval, that included the calculation of the mean and the standard deviation of a set of 10 simulations used to calculate the best model obtained in the inversion process. For simplicity, we selected 4 representative TDEM soundings (5, 10, 15 and 20) for each type of algorithm (WOA, PSO and GWO) with their respective TV and GS constraints. In Table 1 it was depicted the mean and the standard deviation of the resistivity and thickness layers of the model.

Here, it is noted that resistivities and thicknesses for all soundings using the WOA algorithm with GS presented lower values than using the WOA algorithm with TV. These results are quite consistent with those obtained in the inversion process in which the GS constraint favors smooth structures in comparison to the TV constraint. Similarly, the same behavior is reflected for the PSO and GWO algorithms using GS and TV constraints, respectively. In general, it is observed a pattern in which the mean and the standard deviation for each resistivity and thickness of the model are quite close to the mean model obtained and used as a better solution that coherently builds the resistivity model in subsurface. The same procedures and outcomes were obtained for the synthetic model B and field data, but for the sake of simplicity are not shown in this work.

Model B: Buried Valley

Similarly to model A, Figure 3 depicts the inverted resistivity models using TV and GS constraints for the parallelized versions of WOA, PSO and GWO. Both constraints are good approximations to the true model shown in Figure 1b.

To validate these outcomes, as in Model A, we calculated the RE value for the apparent data and inverted model parameters. The outcomes reflect that almost 85% of the inverted model parameters are recovered with a value of RE=15% for the TV constraint (Figure 4c), while 85% of the data are reproduced with lower values of RE=15% for the GS constraint (Figure 4d). It is also noted that almost 85% of the apparent resistivity data are reproduced with RE (%) less than 10% for the TV constraint (Figure 5c), whilst 85% of these parameters are reproduced with RE values lower than 5% for the GS constraint (Figure 5d).

These results conclude that the TV constraint favors solutions in which the physical property of interest has some discontinuities.

In Figure 7, it is depicted the evolution curves of the cost function values. It is also inferred that the best performances are achieved with WOA, and PSO, while the GWO needs a higher number of iterations to achieve the stopping criterion defined in Equation (31).

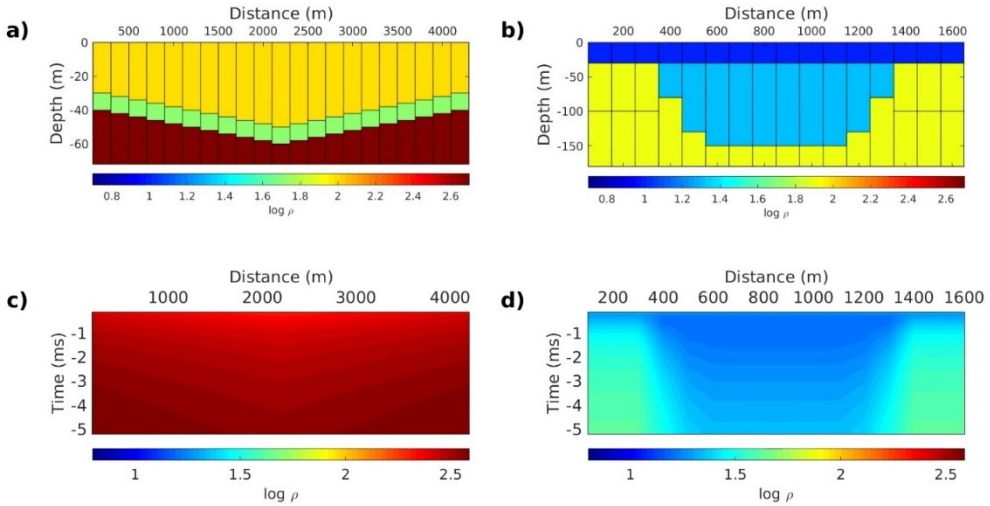

Figure 1: Synthetic data models - (a) True resistivity model A and (b) True resistivity model B. (c) Apparent resistivity section modeled with 21 transient electromagnetic soundings equally spaced (250 m apart), (d) Apparent resistivity section modeled with 16 transient electromagnetic soundings equally spaced (100 m apart).

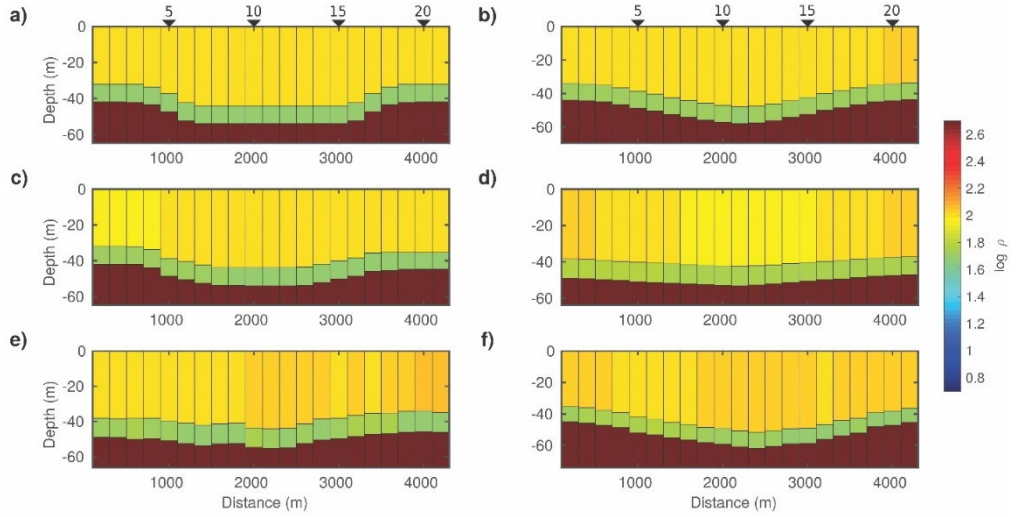

Figure 2: Model A. Inversion outcomes estimated using WOA in a) and b), PSO in c) and d), and GWO in e) and f). The left and right columns show inversion results using TV and GS constraints, respectively.

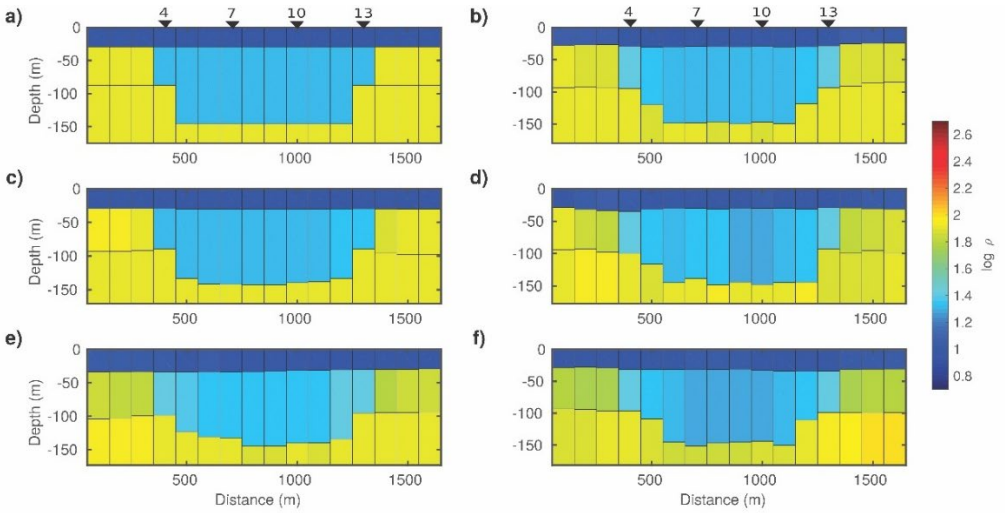

Figure 3: Model B. Inversion outcomes estimated using WOA in (a) and (b), PSO in (c) and (d), and GWO in (e) and (f). The left and right columns show inversion results using TV and GS constraints, respectively.

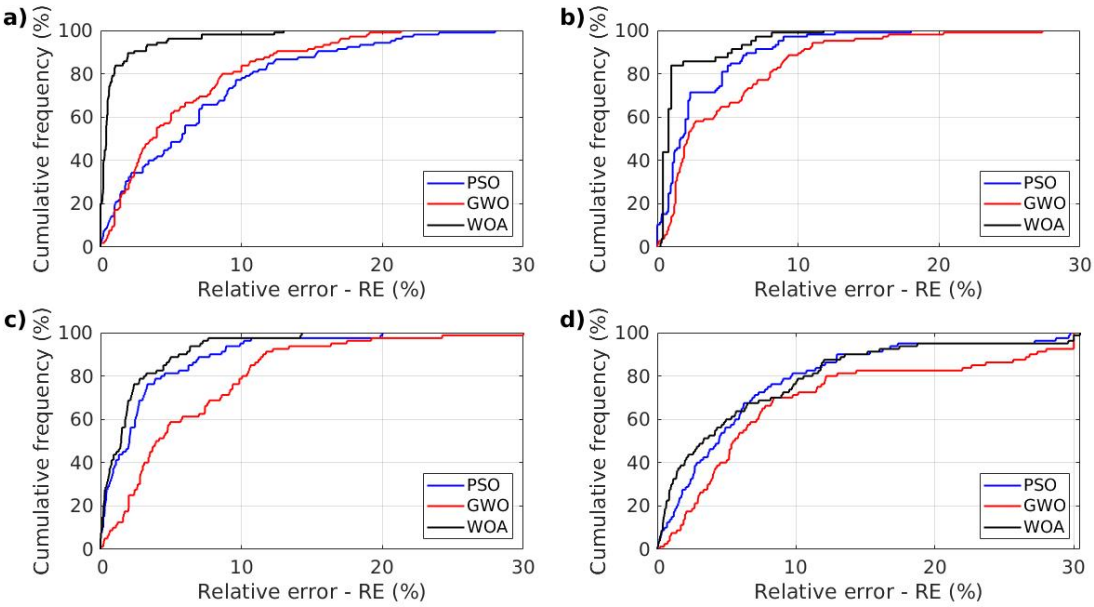

Figure 4: Cumulative distribution for the percentage discrepancy between true model A and the estimated model parameter values in (a) and (b) and for model B in (c) and (d), obtained with WOA, PSO and GWO. The left and right panels are associated with the inversion results using TV and GS constraints, respectively. These outcomes were calculated using the best estimates shown in Figure 2 and Figure 3 for models A and B, respectively

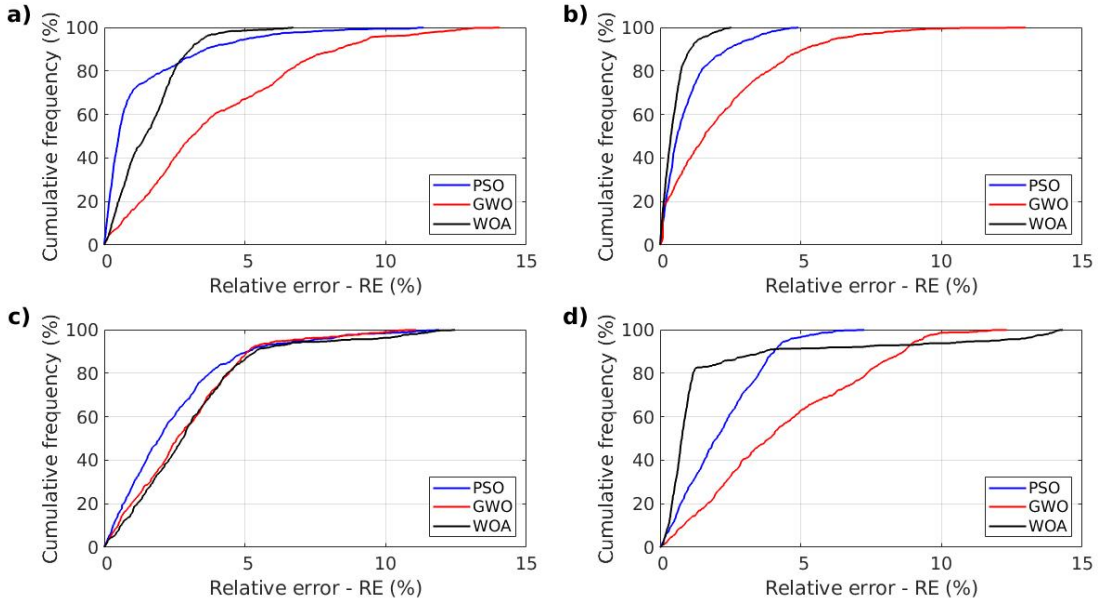

Figure 5: Cumulative distribution for the percentage discrepancy between observed and modeled apparent resistivity data for model A (a) and (b), and for model B (c) and (d), obtained with WOA, PSO and GWO. The left and right panels are associated with the inversion results using TV and GS constraints, respectively. These outcomes were calculated using the best estimates shown in Figure 2 and Figure 3 for models A and B, respectively.

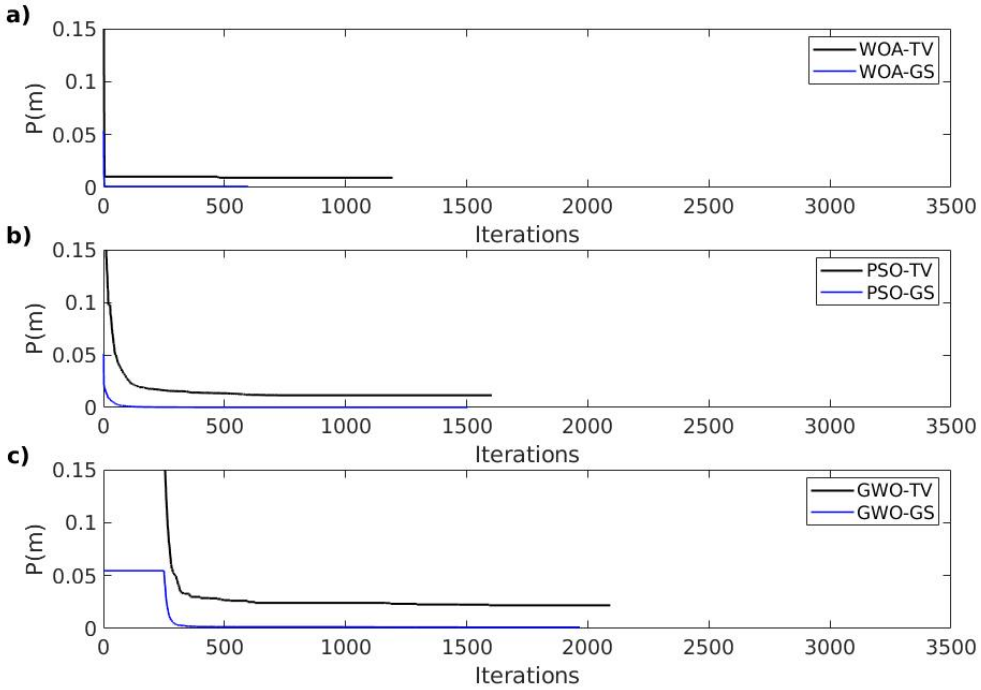

Figure 6: Evolutions of the cost function value along the stages for model A, using TV and GS constraints for the (a) WOA, (b) PSO and (c) GWO methods associated with the respective inversion estimates shown in Figure 2.

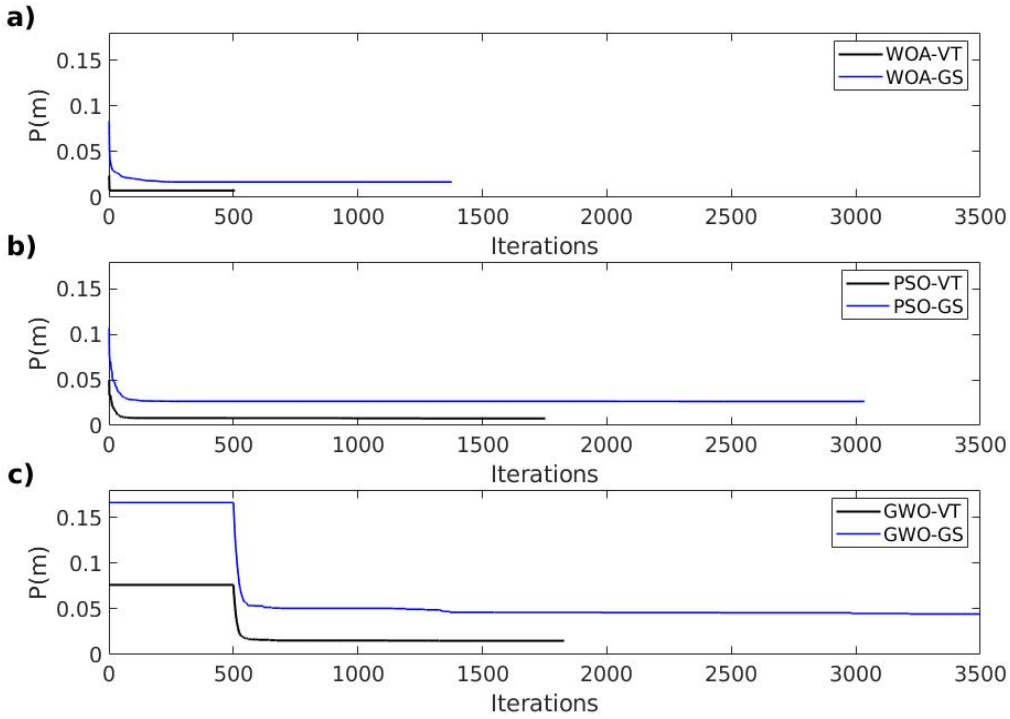

Figure 7: Evolutions of the cost function value along the stages using TV and GS constraints for the (a) WOA, (b) PSO and (c) GWO methods associated with the respective inversion estimates shown in Figure 3.

Table 1: a comparative calculation of the mean and standard deviation for the resistivity and thickness layers belonging to the WOA, PSO and GWO algorithms using TV and GS constraints for the 5, 10, 15 and 20 soundings of model A.

Model A	Sounding	Mean ± standard deviation (sd)				
		ρ_1	ρ_2	P_3	h_1	h_2
WOA TV	5	100.7 ±2.4052	50.34±1.2075	502.72±9.946	38.40±2.2372	10.22±0.5495
	10	100.7 ±2.4052	50.34±1.2075	502.72±9.946	47.86±3.003	10.22±0.5495
	15	100.7 ±2.4052	50.34±1.2075	502.72±9.946	43±1.2981	10.22±0.5495
	20	100.7 ±2.4052	50.34±1.2075	502.72±9.946	32.9±2.9883	10.22±0.5495
WOA GS	5	99.9±0.7746	50.0±0.4123	500.56±2.495	38.18±0.6099	9.98±0.1095
	10	98.28±2.7004	49.72±0.6261	498.74±5.2027	45,74±2.3702	9.98±0.1095
	15	99.58±1.2696	50.06±0.5505	500.45±2.3797	41.68±0.9757	9.98±0.1304
	20	101.70±2.2989	50.02±0.5167	504.96±3.5367	34.16±1.6025	9.96±0.1140
PSO TV	5	102.90±4.2708	48.38±2.8155	496.32±9.4403	38.74±1.7097	9.94±0.4278
	10	100.6±30.0307	46.72±2.8226	496.88±7.4991	44.06±2.0513	10.26±0.5128
	15	101.44±3.2906	46.48±2.8534	503.04±5.4165	41.26±2.0379	9.92±0.7596
	20	101±3.9762	48.16±2.4745	515.22±9.7911	37.38±2.9845	9.44±0.4980
PSO GS	5	99±0.6442	53.18±3.5892	498.58±5.049	39.14±0.7635	9.9±0.5568
	10	96.72±3.6458	50.54±3.8214	493.2±5.7693	44.46±2.6661	10.18±0.7155
	15	96.24±3.5767	51.68±2.9927	506.12±9.44	40.56±1.3353	10.08±0.7497
	20	102.12±5.2841	54.44±5.152	499.40±9.455	35.12±1.8512	10.02±0.3701
GWO TV	5	108.07±8.2468	53.825±2.77	520.40±9.0207	37.675±3.44442	11.975±0.75
	10	108.1±5.1839	51.625±2.9228	532.45±9.1318	54.025±9.1289	11.425±1.0436
	15	110.875±8.1308	52.775±2.7183	511.72±9.262	44.30±6.2944	11.425±0.3594
	20	110.1±9.2869	55.15±7.892	527.27±9.3	35.925±5.471	12.475±1.0372
GWO GS	5	102.675±4.3584	53.85±3.2337	505.8±9.258	40.55±3.061	11.10±0.8756
	10	107±7.17	51.725±0.9032	506.55±9.697	50.47±1.926	11.575±1.513
	15	103.375±2.6924	55.275±5.8375	537.1±9.1766	47.975±6.4598	11.8±1.5556
	20	109.8±6.6458	57.2±7.0781	523.8±9.3844	39.9±5.0971	12.1±2.273

Field data

We used experimental data of TDEM soundings from a survey carried out in 2010 in the city of Bebedouro, São Paulo state, in Brazil (Bortolozo et al., 2014). From this survey, we chose eight TDEM soundings that are approximately aligned forming a transverse (Figure 8a). The TEM survey was conducted with the central-loop array, with square loops with 100m sides. It was used the TEM system from the GEONICS Limited and the TEM-57-MK2 transmitter, with a maximum current of 28A (Geonics, 1994), and the PRO-TEM receiver. The PROTEM receiver works with 20 channels in the turn-off regimes. The frequency range used was 3Hz, 7.5Hz, and 30Hz, which allows three depth investigation levels (30Hz is the shallowest and 3Hz the deepest), providing a time range of investigation from 0.088 to 33.73ms. The data points were then integrated, and the outliers were removed. According to Porsani et al. (2012), this survey was done for better understanding the hydrogeologic setting of fractured basaltic and sedimentary aquifers in the region.

It is worth to mention that there are three principal geological formations in this area: (i) an upper layer that is Adamantina Formation, with approximate thickness that varies from 50 to 100 m, (ii) an intermediate layer made up by the Serra Geral Formation, composed by fractured basalt, with approximate thicknesses that varies from 400 to 600 m (Giampá and de Souza, 1982), and (iii) the bottom layer that corresponds to the Botucatu Formation, which involves the Guarani Aquifer.

In Figure 8b it is shown the PSA borehole, located near to the transverse of TDEM soundings. This well exhibits an intermediate layer composed by fractured basalt, that extends from 50 m to 170 m of depth. Above this layer, it is noted a sedimentary layer that comprises the Adamantina Formation, with an approximate thickness of 50 m. These records allow us to support the geological setting above mentioned. The interpretation results of Bortolozo et al. (2014) to the transverse TDEM soundings are depicted in Figures 9a and 10b. We used an interpretation model of 4 layers according to the results obtained by Bortolozo et al. (2014). Thus, the inversion outcomes were interpreted using 56 parameters.

Figures 9 and 10 show the inversion results obtained using TV and GS constraints with WOA, PSO and GWO, respectively. Both constraints reproduce quite well the solution of Bortolozo et al. (2014) with few differences. The principal discrepancy occurs between the T77 and T79 soundings. It seems that a fault affects the basalt layer of the Serra Geral Formation (yellow to orange color) at a depth of 100 m. It is also noted in all inversion results that the TV constraint identified this abrupt discontinuity better than the GS constraint.

To crosscheck the quality of the inversion estimates obtained with both constraints, we performed a statistical analysis of the cumulative frequency distribution of the relative errors of all inversion results. These outcomes showed that almost 95% of the apparent resistivity data are reproduced with values less than RE=20% for the TV constraint (Figure 11a), whilst 95% of the data are reproduced with RE lower than 30% for the GS constraint (Figure 11b). It is also noted that the WOA and PSO exhibit better performances than the GWO. This last information is also validated in Figure 12, where the WOA needed fewer iterations to achieve the termination criterion than the PSO and GWO algorithms. It is also noted that the TV constraint in all cases exhibited better results than the GS constraint.

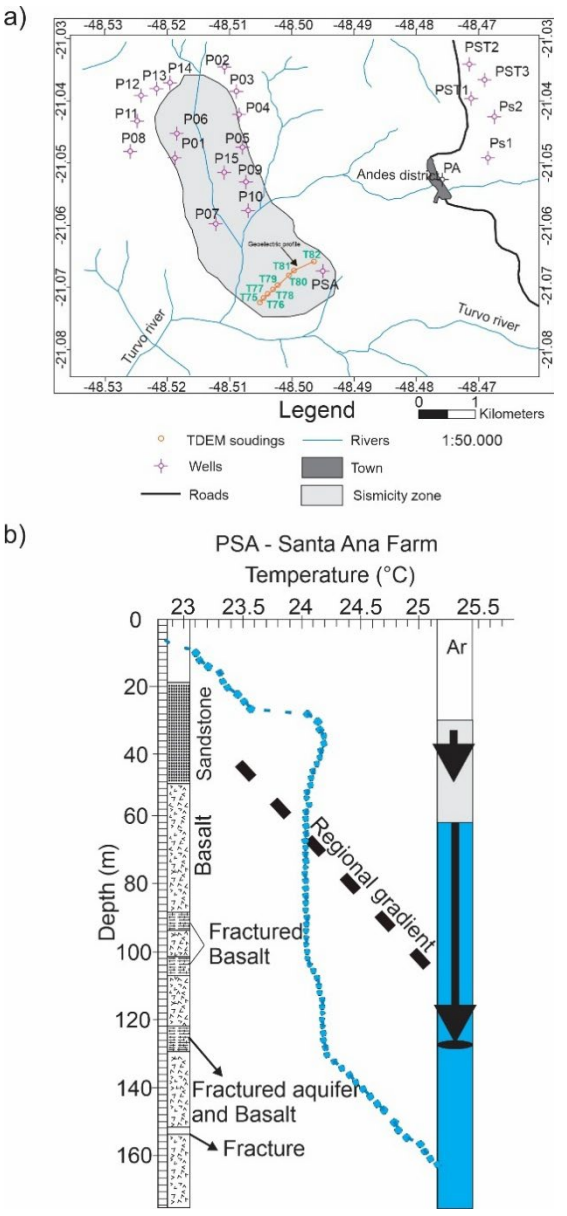

Figure 8: (a) TDEM soundings surveyed in Bebedouro city. In orange it is the geoelectric profile containing the 8 soundings (T75-T82) used in this work. Adapted from Bortolozo et al. (2014). (b) Thermal well PSA located in Santa Ana Farm, near to the line of TDEM soundings. The depth of the fractured basalt is shown from 50 m approximately. Adapted from Assumpção et al. (2010).

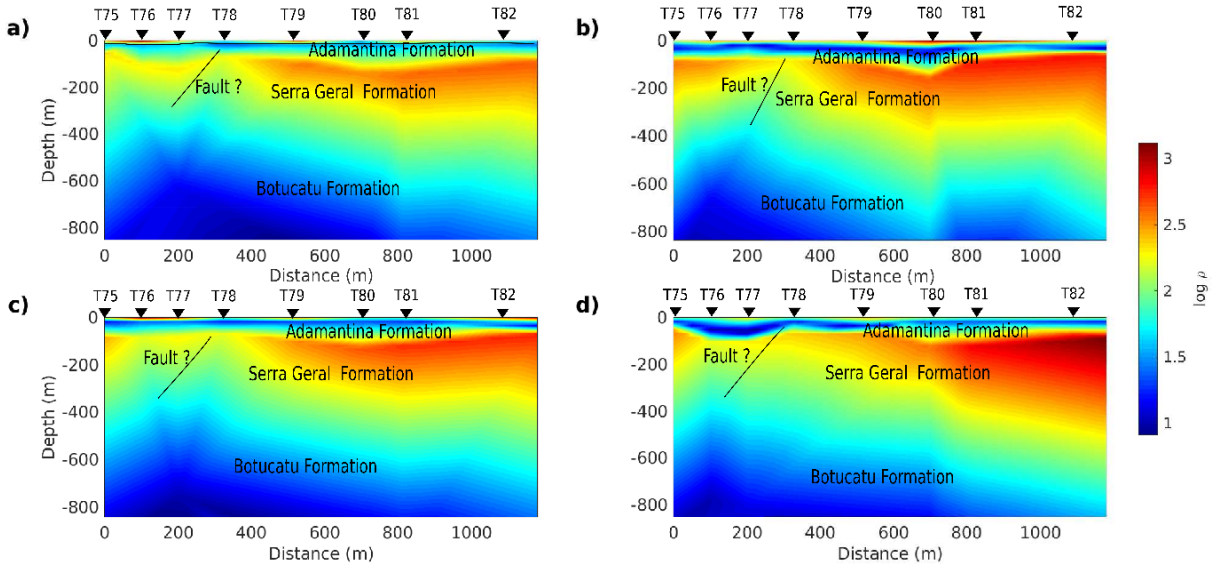

Figure 9: Field data. (a) Solution of Bortolozo et al. (2014). (b), (c) and (d) The inversion obtained with PSO, GWO and WOA, respectively, using TV constraint. The color bar that represents the resistivity value is the same in all figures.

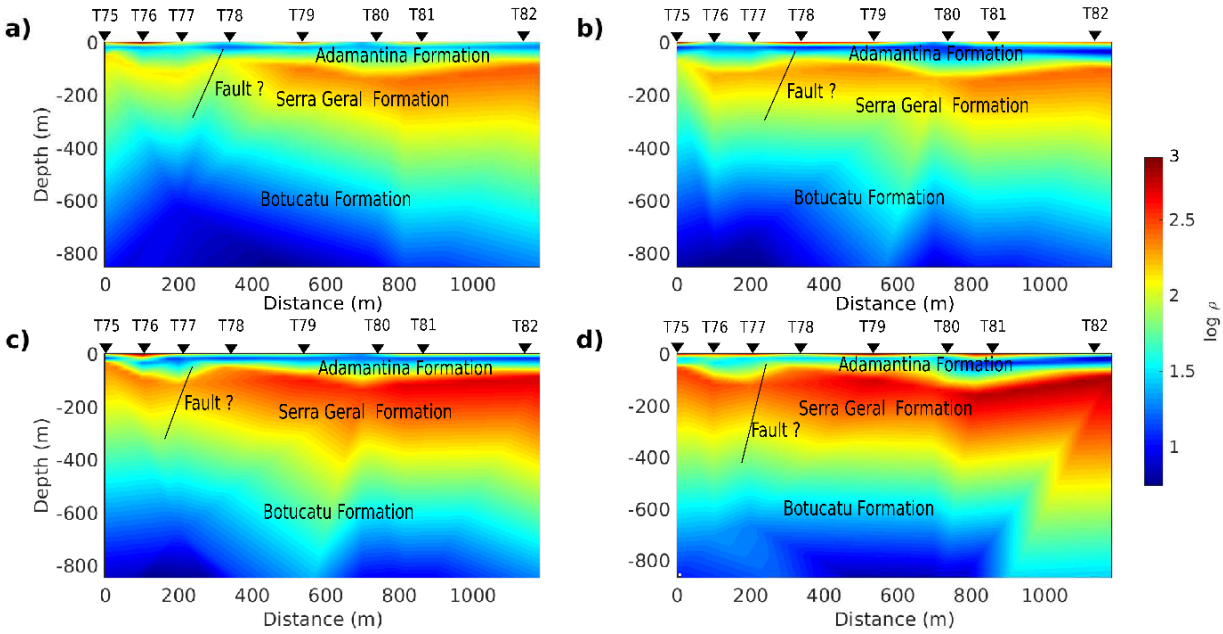

Figure 10: Field data. (a) Solution of Bortolozo et al. (2014). (b-d) The inversion obtained with PSO, GWO and WOA, respectively, using GS constraint. The color bar that represents the resistivity value is the same in all figures.

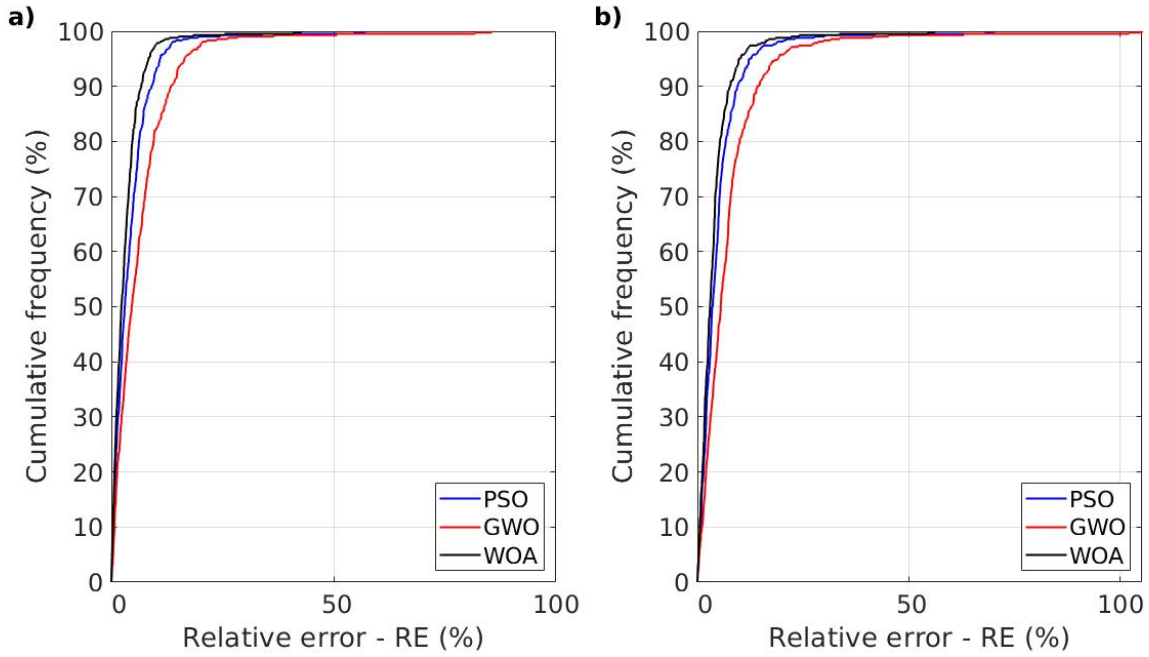

Figure 11: Cumulative distribution for the percentage discrepancy between observed and modeled apparent resistivity data for the Bebedouro area with the three methods, using TV constraint (a) and using GS constraint (b). These outcomes were calculated using the best inverted models obtained for PSO, GWO and WOA, respectively.

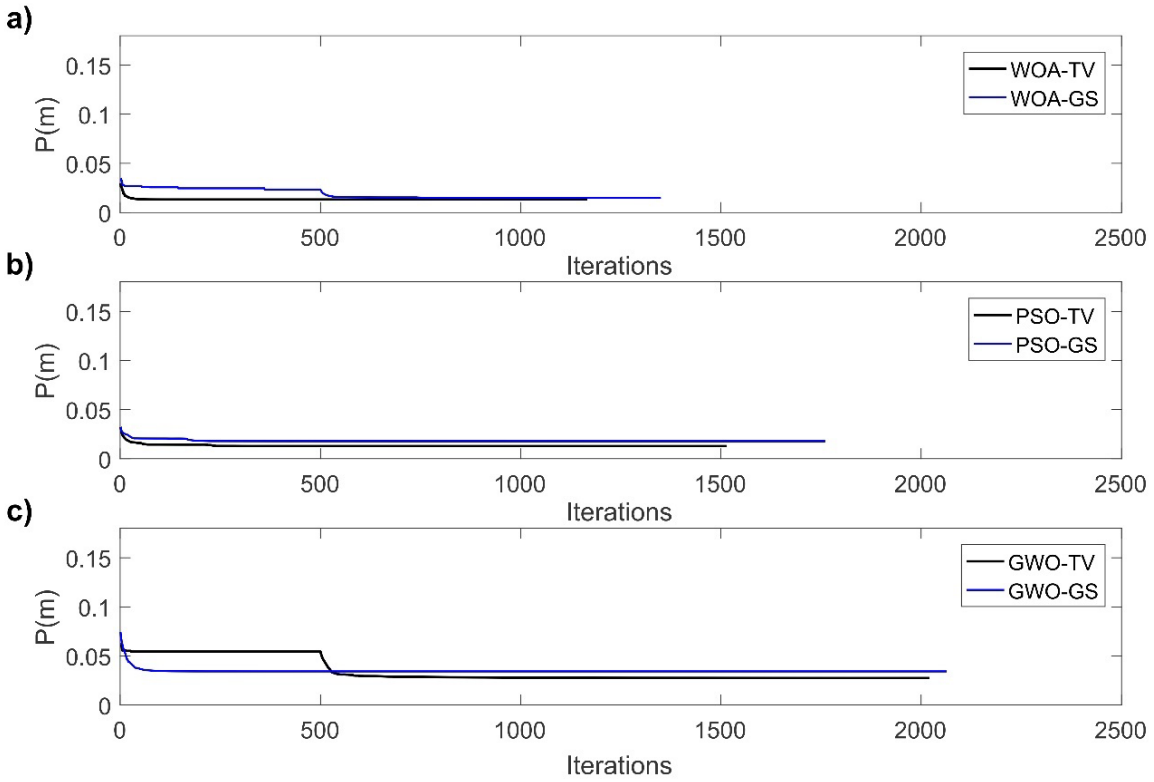

Figure 12: Field data. Evolution of the cost function value along the stages using TV and GS constraints for the (a) WOA, (b) PSO and (c) GWO methods associated with the respective inversion estimates shown in Figures 9 and 10.

DISCUSSION

GOMs offer high flexibility to incorporate several kinds of constraints once they are implemented computationally. This vantage offers an easy way to the interpreter to establish possible characteristics about the electrical resistivity distributions on the subsurface. In this work, we compare two lateral continuity constraints such as TV and GS on the model parameters as a manner to determine localized discontinuities such as sharp structures and faults. These constraints were incorporated easily in classical versions of WOA, PSO and GWO. However, these techniques require a high computational cost associated with the huge quantity of cost function evaluations (Sen et al., 1993). As a manner of overcoming this disadvantage, several approaches adopting parallel architectures and programming languages have been used in the last years (e.g., Lalwani et al., 2019).

Such parallel techniques allow reducing the inversion time enormously. Table 2 presents a quantitative distribution of such reduction in time, taking as a pattern the serial processing time. For the performance tests, we ran the inversions with both synthetic models and real data. We tested all parallelized versions of WOA, PSO and GWO on a high-performance cluster for scientific computing. Each CPU model of a cluster node is a 2.3 GHz Intel Xeon Sixteen-Core E5-2698v3 with 128 GB RAM. We used 32 MPI processes per node, that provided the best performance, reducing the computational time significantly. The pure MPI version achieved a 17x speed-up (quotient between the sequential time execution and the parallel execution time) for both synthetic models and a 50x speed-up for the real data.

In summary, both synthetic models and real data had better performances with the GS constraint, very useful to determine sharp structures and faults. Figure 9 is a good example of that, where the inverted model parameters reproduced well fractured basalt layer below soundings (T77-T79). In the same way, Figure 3 proved to be efficient to localize sharp contacts and alternation of materials resulting from buried valleys. This evidence supports the fact that the GS constraint is more sensitive to the model, principally to high-low variations of resistivity (Menke, 2018).

CONCLUSIONS

In this study, we compare the performances of three GOMs to solve the 1.5D TEM inverse problem using synthetic and real data. These techniques offer high flexibility in incorporating different constraints in the cost function, but present some drawbacks, such as rapid entrapment in local minimum and high computational cost. To mitigate the latter disadvantage, we made a parallelization for the classical versions of WOA, PSO and GWO. This implementation is based on the master/worker paradigm of parallel processing, in which the master process performs WOA-related operations, PSO and GWO, and the worker processes complete the evaluation of the agents. The pure MPI version demonstrated to be highly effective in the reduction of computational time for all simulations. We validate the parallelized versions of WOA, PSO and GWO in both synthetic models and the experimental data using a statistical analysis of cumulative distribution frequency of relative errors for apparent resistivity data and inverted model parameters. Both solutions provide good results and turn into an excellent alternative to the classical inversion techniques of time electromagnetic data.

AVAILABLE CODES

The codes can be available upon request to the main authors.

Table 2: Total execution time comparison between parallel (MPI) and sequential inversions.

Model	Algorithm	Parallel processing (MPI)		Sequential processing	
		TVC	GSC	TVC	GSC
Model A	WOA	2.14 hr	1.06 hr	36.8 hr	18.44 hr
	PSO	3.8 hr	3.03 hr	68.9 hr	52.8 hr
	GWO	6.5 hr	3.64 hr	115.3 hr	64.8 hr
Model B	WOA	0.57 hr	1.58 hr	9.92 hr	27 hr
	PSO	2.06 hr	3.6 hr	35.13 hr	62.53 hr
	GWO	2.08 hr	4.2 hr	36.1 hr	71.42 hr
Bebedouro	WOA	0.32 hr	0.48 hr	16.19 hr	24.4 hr
	PSO	0.42 hr	0.57 hr	21.02 hr	28.65 hr
	GWO	0.5 hr	0.63 hr	25.06 hr	31.93 hr

ACKNOWLEDGMENTS

Jorge Abril acknowledges the Coordenação de Aperfeiçoamento de Pessoal de Nível Superior (CAPES) - Brasil - Finance Code 001 for his PhD scholarship. Cassiano Bortolozo thanks to Conselho Nacional de Desenvolvimento Científico e Tecnológico (CNPq) for the Postdoctoral Scholarship (grant 152269/2022-3), for the Research Fellowship Program (grant 301201/2022-6) and also for the Research Financial Support (Universal Project grant 433481/2018-8). Cassiano Bortolozo also thanks to Fundação de Amparo à Pesquisa do Estado de São Paulo (FAPESP) for the scholarship (grant 2011/06404-0) that allowed the data acquisition. The authors also thank to Núcleo de Processamento de Alto Desempenho (NPAD) of Universidade Federal do Rio Grande do Norte (UFRN) for the provision of computational resources for this research.

REFERENCES

Abdelazeem, M., M. Gobashy, M.H. Khalil, and M. Abdrabou, 2019, A complete model parameter optimization from self-potential data using Whale algorithm: Journal of Applied Geophysics, **170**, 103825, doi: 10.1016/j.jappgeo.2019.103825.

Agarwal, A., A. Chandra, S. Shalivahan, and R.K. Singh, 2018, Grey wolf optimizer: a new strategy to invert geophysical data sets: Geophysical Prospecting, **66**, 6, 1215–1226, doi: 10.1111/1365-2478.12640.

Anderson, W.L., 1982, Calculation of transient soundings for a coincident loop system (Program TCOLOOP): U.S. Geological Survey, Open-File Report 82-378, 77 p, doi: 10.3133/ofr82378.

Assumpção, M., T.H. Yamabe, J.R. Barbosa, V. Hamza, A.E.V. Lopes, L. Balancin, and M.B. Bianchi, 2010, Seismic activity triggered by water wells in the Paraná Basin, Brazil: Water Resources Research, **46**, 7, W07527, doi: 10.1029/2009WR008048.

Auken, E., and A.V. Christiansen, 2004, Layered and laterally constrained 2D inversion of resistivity data: Geophysics, **69**, 3, 752–761, doi: 10.1190/1.1759461.

Auken, E., A.V. Christiansen, B.H. Jacobsen, N. Foged, and K.I. Sørensen, 2005, Piecewise 1D laterally constrained inversion of resistivity data: Geophysical Prospecting, **53**, 4, 497–506, doi: 10.1111/j.1365-2478.2005.00486.x.

Auken, E., A.V. Christiansen, L.H. Jacobsen, and K.I. Sørensen, 2008, A resolution study of buried valleys using laterally constrained inversion of TEM data: Journal of Applied Geophysics, **65**, 1, 10–20, doi: 10.1016/j.jappgeo.2008.03.003.

Barboza, F.M., W.E. Medeiros, and J.M. Santana, 2018, Customizing constraint incorporation in direct current resistivity inverse problems: A comparison among three global optimization methods: Geophysics, **83**, 6, E409–E422, doi: 10.1190/geo2017-0188.1.

Bartle, R.G. 1964. The elements of real analysis: vol 2, John Wiley & Sons, New York.

Bertete-Aguirre, H., E. Cherkaev, and M. Oristaglio, 2002, Non-smooth gravity problem with total variation penalization functional: Geophysical Journal International, **149**, 2, 499–507, doi: 10.1046/j.1365-246X.2002.01664.x.

Bortolozo, C.A., M.A. Couto Jr., J.L. Porsani, E.R. Almeida, and F.A.M. dos Santos, 2014, Geoelectrical characterization using joint inversion of VES/TEM data: A case study in Paraná Sedimentary Basin, São Paulo State, Brazil: Journal of Applied Geophysics, **111**, 33–46, doi: 10.1016/j.jappgeo.2014.09.009.

Chandra, A., A. Agarwal, and R.K. Singh, 2017, Grey wolf optimisation for inversion of layered earth geophysical datasets: Near Surface Geophysics, **15**, 5, 499–513, doi: 10.3997/1873-0604.2017017.

Chen, W., H. Hong, M. Panahi, H. Shahabi, Y. Wang, A. Shirzadi, S. Pirasteh, A.A. Alesheikh, K. Khosravi, S. Panahi, F. Rezaie, S. Li, A. Jaafari, D.T. Bui, and B. Bin Ahmad, 2019, Spatial prediction of landslide susceptibility using GIS-based data mining techniques of ANFIS with Whale Optimization Algorithm (WOA) and Grey Wolf Optimizer (GWO): Applied Sciences, **9**, 18, 3755, doi: 10.3390/app9183755.

Cheng, J., F. Li., S. Peng, X. Sun, J. Zheng, and J. Jia, 2015, Joint inversion of TEM and DC in roadway advanced detection based on particle swarm optimization: Journal of Applied Geophysics, **123**, 30–35, doi: 10.1016/j.jappgeo.2015.09.008.

Christensen, N.B., 1990, Optimized fast Hankel transform filters: Geophysical Prospecting, **38**, 5, 545–568, doi: 10.1111/j.1365-2478.1990.tb01861.x.

Clerc, M., 1999, The swarm and the queen: towards a deterministic and adaptive particle swarm optimization: 1999 Congress on Evolutionary Computation-CEC99 (Cat. No. 99TH8406), IEEE, p 1951–1957.

Cockett, R., S. Kang, L.J. Heagy, A. Pidlisecky, and D.W. Oldenburg, 2015, SimPEG: An open source framework for simulation and gradient based parameter estimation in geophysical applications: Computers & Geosciences, **85**, 142–154, doi: 10.1016/j.cageo.2015.09.015.

Constable, S.C., R.L. Parker, and C.G. Constable, 1987, Occam's inversion: A practical algorithm for generating smooth models from electromagnetic sounding data: Geophysics, **52**, 3, 289–300, doi: 10.1190/1.1442303.

deGroot-Hedlin, C., and S. Constable, 1990, Occam's - models from magnetotelluric data: Geophysics, **55**, 12, 1613–1624, doi: 10.1190/1.1442813.

Engelbrecht, A.P., 2007, Computational Intelligence: An Introduction: 2nd ed., John Wiley & Sons, 640 pp, doi: 10.1002/9780470512517.

Geonics, 1994, PROTEM-47D, Operating Manual: Geonics Limited, Mississauga, Ontario, Canada.

Giampá, C.E.Q., and J.C. de Souza, 1982, Potencial aquífero dos basaltos da Formação Serra Geral no Estado de São Paulo: 2º Congresso Brasileiro de Águas Subterrâneas, ABAS, Salvador, BA, Brazil.

Gill, P.E., W. Murray, and M.H. Wright, 2019, Practical optimization: Classics in Applied Mathematics, SIAM, 401 pp, doi: 10.1137/1.9781611975604.

Godio, A., and A. Santilano, 2018, On the optimization of electromagnetic geophysical data: Application of the PSO algorithm: Journal of Applied Geophysics, **148**, 163–174, doi: 10.1016/j.jappgeo.2017.11.016.

Goldberg, D., 1989, Genetic algorithms in search, optimization, and machine learning: Addison-Wesley, Boston, MA, USA, 372 pp.

Hansen, P.C., 1992, Analysis of discrete ill-posed problems by means of the L-curve: SIAM Review, **34**, 4, 561–580, doi: 10.1137/1034115.

Ingeman-Nielsen, T., and F. Baumgartner, 2006, CR1Dmod: A Matlab program to model 1D complex resistivity effects in electrical and electromagnetic surveys: Computers & Geosciences, **32**, 9, 1411–1419, doi: 10.1016/j.cageo.2006.01.001.

Kennedy, J., 2006, Swarm intelligence, *in* Zomaya, A.Y., Ed., Handbook of nature-inspired and innovative computing: Springer, Boston, MA, chapter 6, 187–219, doi: 10.1007/0-387-27705-6_6.

Kennedy, J., and R. Eberhart, 1995, Particle swarm optimization: ICNN'95 - International Conference on Neural Networks, IEEE, Perth, WA, Australia, vol.4, 1942–1948, doi: 10.1109/ICNN.1995.488968.

Kirkpatrick, S., C.D. Gelatt Jr., and M.P. Vecchi, 1983, Optimization by simulated annealing: Science, **220**, 4598, 671–680, doi: 10.1126/science.220.4598.671.

Lalwani, S., H. Sharma, S.C. Satapathy, K. Deep, and J.C. Bansal, 2019, A survey on parallel particle swarm optimization algorithms: Arabian Journal for Science and Engineering, **44**, 2899–2923, doi: 10.1007/s13369-018-03713-6.

Lee, C.-Y., and G.-L. Zhuo, 2021, A hybrid whale optimization algorithm for global optimization: Mathematics, **9**, 13, 1477, doi: 10.3390/math9131477.

Li, S.-Y., S.-M. Wang, P.-F. Wang, X.-L. Su, X.-S. Zhang, and Z.-H. Dong, 2018, An improved grey wolf optimizer algorithm for the inversion of geoelectrical data: Acta Geophysica, **66**, 607–621, doi: 10.1007/s11600-018-0148-8.

Liang, X., S. Xu, Y. Liu, and L. Sun, 2022, A Modified Whale Optimization Algorithm and Its Application in Seismic Inversion Problem: Mobile Information Systems, **2022**, 9159130, 1–18, doi: 10.1155/2022/9159130.

Loke, M.H., I. Acworth, and T. Dahlin, 2003, A comparison of smooth and blocky inversion methods in 2D electrical imaging surveys: Exploration Geophysics, **34**, 3, 182–187, doi: 10.1071/EG03182.

Martínez, J.L.F., E.G. Gonzalo, J.P.F. Álvarez, H.A. Kuzma, and C.O.M. Pérez, 2010. PSO: A powerful algorithm to solve geophysical inverse problems: Application to a 1D-DC resistivity case: Journal of Applied Geophysics, **71**, 1, 13–25, doi: 10.1016/j.jappgeo.2010.02.001.

Menke, W., 2018, Geophysical data analysis: Discrete inverse theory: 4th ed., Academic Press. 352 pp.

Metcalfe, T.S., and P. Charbonneau, 2003, Stellar structure modeling using a parallel genetic algorithm for objective global optimization: Journal of Computational Physics, **185**, 1, 176–193, doi: 10.1016/S0021-9991(02)00053-0.

Mirjalili, S., and A. Lewis, 2016, The Whale Optimization Algorithm: Advances in Engineering Software, **95**, 51–67, doi: 10.1016/j.advengsoft.2016.01.008.

Mirjalili, S., S.M. Mirjalili, and A. Lewis, 2014, Grey wolf optimizer: Advances in Engineering Software, **69**, 46–61, doi: 10.1016/j.advengsoft.2013.12.007.

Monteiro, F.A.S., and H.M. El-Kaliouby, 2010, Comparative study of local versus global methods for 1D joint inversion of direct current resistivity and time-domain electromagnetic data: Near Surface Geophysics, **8**, 2, 135–143, doi: 10.3997/1873-0604.2009056.

Muro, C., R. Escobedo, L. Spector, and R.P. Coppinger, 2011, Wolf-pack (*Canis lupus*) hunting strategies emerge from simple rules in computational simulations: Behavioural Processes, **88**, 3, 192–197, doi: 10.1016/j.beproc.2011.09.006.

Porsani, J.L., E.R. Almeida, C.A. Bortolozo, and F.A.M. dos Santos, 2012, TDEM survey in an area of seismicity induced by water wells in Paraná sedimentary basin, Northern São Paulo State, Brazil: Journal of Applied Geophysics, **82**, 75–83, doi: 10.1016/j.jappgeo.2012.02.005.

Rawlinson, N., A.M. Reading, and B.L.N. Kennett, 2006, Lithospheric structure of Tasmania from a novel form of teleseismic tomography: Journal of Geophysical Research: Solid Earth, **111**, B02301, doi: 10.1029/2005JB003803.

Rudin, L.I., S. Osher, and E. Fatemi, 1992, Nonlinear total variation based noise removal algorithms: Physica D: Nonlinear Phenomena, **60**, 1-4, 259–268, doi: 10.1016/0167-2789(92)90242-F.

Sandberg, S.K., 1988, Microcomputer software for the processing and forward modeling of transient electromagnetic data taken in the central loop sounding configuration: New Jersey Department of

Environmental Protection, Division of Water Resources, New Jersey Geological Survey, Open-File Report 88-1, 88 pp.

Santos, F.A.M., 2004, 1-D laterally constrained inversion of EM34 profiling data: Journal of Applied Geophysics, **56**, 2, 123–134, doi: 10.1016/j.jappgeo.2004.04.005.

Sen, M.K., and P.L. Stoffa, 1995, Global optimization methods in geophysical inversion: Cambridge University Press.

Sen, M.K., and P.L. Stoffa, 2013, Global optimization methods in geophysical inversion: Cambridge University Press, doi: 10.1017/CBO9780511997570.

Sen, M.K., B.B. Bhattacharya, and P.L. Stoffa, 1993, Nonlinear inversion of resistivity sounding data: Geophysics, **58**, 4, 496–507, doi: 10.1190/1.1443432

Silva, J.B., W.E. Medeiros, and V.C. Barbosa, 2001, Potential-field inversion: Choosing the appropriate technique to solve a geologic problem: Geophysics, **66**, 2, 511–520, doi: 10.1190/1.1444941.

Abril-Benjumea, J.L.: code writing, algorithm development, paper first version writing, result interpretation and analysis; **Rodrigues-Vasconcelos, M.:** manuscript revision, result analysis support; **Antônio-Bortolozo, C.:** code elaboration to depict the figures, some result writing, manuscript revision; **Márcio-Barboza, F.:** manuscript revision, result analysis support.

Received on October 17, 2022 / Accepted on April 24, 2023